

# Spin-coating of vertically stratified thin liquid films

A. MCINTYRE<sup>1</sup> AND L. N. BRUSH<sup>2†</sup>

<sup>1</sup>Department of Applied Mathematics, University of Washington, Seattle, WA 98195, USA

<sup>2</sup>Department of Materials Science and Engineering, University of Washington, Seattle, WA 98195, USA

(Received 20 August 2009; revised 29 September 2009; accepted 30 September 2009)

Spin-coating is a process used to fabricate thin films for device applications. In this paper, lubrication theory is used to derive an axisymmetric model for the spin-coating of two immiscible vertically stratified Newtonian thin films. The model includes gravitational, van der Waals, capillary and viscous forces, differences in liquid layer properties and evaporation/condensation effects. Thinning calculations focus on the effects of viscosity and condensation/evaporation. In this case, for layers of uniform thickness, the lower layer thins monotonically yet never reaches zero thickness. With evaporation mass loss the upper layer disappears in finite time, whereas with condensation effects the upper layer approaches a steady-state thickness. Fully nonlinear calculations are carried out for films with non-uniform thickness and the deviation of the interfaces from the flat state is monitored. In general, disturbances to the lower layer have a greater effect on the upper layer than those of disturbances of the upper layer on the lower layer. Disturbances along the upper gas–liquid free surface propagate outward more rapidly than those along the lower liquid–liquid interface and disturbances that decrease the film thickness tend to dissipate more slowly.

---

## 1. Introduction

Spin-coating is a common material processing technique used to create thin films. It is accomplished by pouring liquid material on to a substrate, the rotation of which causes the liquid to spread and thin over the substrate until a target thickness is reached. Spin-coating is used to process semiconductors, DVDs and CDs, among other devices (Momoniat & Mason 1998; Charpin, Lombe & Myers 2007). Now spin-coating can be used to produce layers as thin as tens of nanometres; therefore there has been the recent application of spin-coating technology during the processing of other advanced devices. For example, the spin-coating of polymer blends and conjugated polymers is used in the production of light-emitting diodes (LEDs), thin-film transistors (TFTs), electrochromic cells and photovoltaic devices. (Wei, Coffey & Ginger 2006; Castro *et al.* 2007).

Polymers are used because they are cheap to process compared with other materials, and they can be designed for a variety of configurations. Also, in a polymer blend there can be phase separation resulting in the development of internal microstructure or even nanostructure during spin-coating (Halls *et al.* 1995; Castro *et al.* 2007).

† Email address for correspondence: brush@u.washington.edu

In photovoltaic devices, development of methods to achieve these structures is the focus of current research efforts, since the nanostructure must be fine enough (tens of nanometres; Yang & Forrest 2008; Jen, personal communication) in order to generate electricity. Control over the thinning process and phase separation in polymers or in any other material is important in enabling the production of films with tailored properties. However, phase separation is very difficult to control, and better understanding of the evolution of the nanostructure as a function of the variables in the spin-coating process is needed.

There are different proposed mechanisms for the evolution of the nanostructures/microstructures in polymer blends during spin-coating. One mechanism is the direct separation of phases via a spinodal or nucleation and growth route. Phase separation simply occurs in the bulk at the same time the film is thinning. The evolving liquid–liquid or gas–liquid interface bounding the thinning film is not required for internal phase separation (Heriot & Jones 2005). However, it is also the case that phase separation in blends can occur unidirectionally, parallel to the substrate surface, resulting in a vertically layered structure. Often, chemically treated substrates are used to generate vertically layered structures during spin-coating (Bjorstrom *et al.* 2007). Heriot & Jones (2005) have provided experimental evidence supporting an interfacial-driven mechanism of phase separation in a polymer blend of polymethylmethacrylate (PMMA) and polystyrene (PS) that destroys the bilayer structure under certain conditions. In this work, time-resolved small-angle light scattering and light reflectivity were used to observe *in situ* the evolution of the nanostructure during spin-coating. The results indicate that the blend of polymers separates into a vertically layered two-phase structure so that there is a horizontal (or a nearly horizontal) polymer–polymer interphase boundary. This interface then undergoes an instability which evolves into the final nanostructure. Typical experimental results of Heriot & Jones (2005) illustrate film thicknesses in the range of tens to a thousand nanometres, whereas in the lateral or longitudinal direction the structure has a characteristic dimension of 1–50 microns. In addition, Sprenger *et al.* (2003) have outlined different methods for the creation of hierarchical patterns in spin-coated polymers, including polymer phase separation into a bilayer structure followed by an interfacial instability. They were able to select the route by varying the spin-coating speed and the concentration of the solution.

The interfacial instability in the thin multi-layered spin-coated film can occur at very low Reynolds number. Thin liquid films are subject to a variety of intermolecular forces, the strength of which depends on the nature of the liquid and the phases bounding the liquid as well as the thickness of the film (see, for example, Israelachvili 1991). The origin of the interfacial instability could be the intermolecular forces which become increasingly important as any film thins to within a couple of hundred nanometres. The study of the effects of van der Waals forces on stability of static thin films has been carried out by Williams & Davis (1982) and in free films by Erneux & Davis (1993). Many other researchers have also studied these intermolecular forces in a variety of films as the reviews by Davis (1995), Oron, Davis & Bankoff (1997) and Craster & Matar (2009) well describe.

Other mechanisms giving rise to interfacial instabilities have also been identified in layered fluids at very low Reynolds number that are not related to the thin-film forces discussed above. Li (1969) and Kliakhandler & Sivashinsky (1995, 1996) have shown that there are long-wave interfacial instabilities in stratified three-layer creeping Couette flows in which inertial effects play no role. Gao & Lu (2008) examined an interfacial instability in a tilted two-layered liquid in which there are gravitational forces driving a flow in the longitudinal direction and in which inertia again plays no

role. They suggest that the behaviour of the jumps in the flow and pressure fields at the free surface and at the internal interface is the source of the mechanism driving the instability.

In summary, the conclusion from previous research efforts is that there may be different mechanisms responsible for the evolution of the nanostructure observed in spin-coated polymer blends. Of interest here is the initial stratification of the polymers into a two-layered structure, followed by a hydrodynamically driven interfacial instability, which results in a two-phase mixture.

In this paper lubrication theory is used to develop a model for the spin-coating of a two-layer liquid. The initial condition for the model is two immiscible, vertically stratified liquid layers with a passive gas above. In the model, the fluids are assumed to be Newtonian, each having constant density and viscosity but differing from one phase to another. The model derived includes the effects of gravity, van der Waals forces, capillary forces and viscous forces as well as those of mass loss/gain because of evaporation/condensation along the upper free surface. However, in this paper the calculations only include the effects of viscosity and evaporation; other effects will be considered later. The overall purpose of this work is to examine how a two-layer system evolves during spin-coating, including observing whether or not there are interfacial instabilities unique to a two-layer system, and to understand how evolving disturbances on one interface affect evolution of the other interface. Before presenting the model, relevant modelling efforts in spin-coating are discussed.

### 1.1. *Modelling efforts in spin-coating*

One of the earliest efforts in spin-coat modelling was carried out by Emslie, Bonner & Peck (1958). They applied lubrication theory to model a Newtonian liquid thinning on a rotating disk at low Reynolds number, meanwhile ignoring gravitational, capillary forces and Coriolis effects. Using the method of characteristics, they were able to examine the evolution of a variety of initial interfacial profiles. In general they found that spinning leads to evening of surfaces over time, although there were some cases in which this appeared not to be true, but as they stated, in those instances, the theory breaks down.

Reisfeld, Bankoff & Davis (1991a) examined the spin-coating of a thin liquid film on a substrate. They also used lubrication theory to derive the governing equations including centripetal, inertial, surface tension and gravitational forces as well as evaporation and condensation at the free surface. They computed the rates of uniform film thinning because of radial drainage. They found that evaporation causes a film to thin to zero thickness in finite time. With condensation steady-state thicknesses can be achieved, owing to a balance between the mass lost from radial drainage and mass gained because of condensation. They investigated the linear stability of the film and concluded that for evaporating surfaces the lower-wavenumber disturbances are stable and the larger-wavenumber ones are transiently stable. Condensing films show regions of instability at larger wavenumbers in addition to stable and transiently stable ranges.

Subsequently, Reisfeld, Bankoff & Davis (1991b) explored the evolution of disturbances in a multicomponent film. They derived coupled nonlinear evolution equations for the height of the film and for the concentration field within the film. Their findings showed that interfaces exhibited irregularities in the case in which the fluids had highly volatile solvents, which is consistent with experiment.

Recent highlights of other spin-coat modelling efforts include the work of Schwartz & Roy (2004) who developed a quite general model for the spin-coating

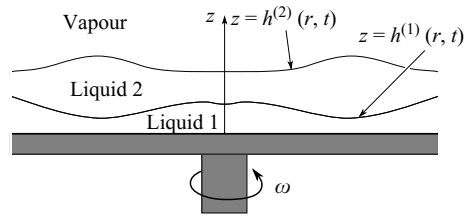


FIGURE 1. Schematic representation of rotating liquid films.

of a Newtonian liquid film using lubrication theory. Their model includes surface tension, gravity and van der Waals forces, chemically patterned substrates and a finite contact angle at the leading edge of the thinning film. Their numerical results showed that the reason for finger formation at the leading edge of spinning films was imperfect wetting behaviour, in good agreement with experiment. They also argued that for spin-coating problems the static equilibrium contact angle can be used to accurately model the behaviour of the film. They claimed that the dynamic contact angle relationships (Dussan & Davis 1974; Dussan 1979; Ehrhard & Davis 1991) are not required for spin-coat models.

More recently Charpin *et al.* (2007) have studied the spin-coating of generalized Newtonian films using the power-law and Ellis-law models of the viscosity. The Ellis model exhibits Newtonian behaviour up to a transition value in the shear rate, and then for higher shear rates there is power-law dependence. Power-law fluids show a spike in the centre of the film because of the vanishing of the shear rate there and thus an infinite viscosity. Capillarity eliminates this spike. The Ellis model also has a central spike, but it is smoother, and the film spreads more rapidly than in the power-law model. Similar power-law behaviour had been observed by Acrivos, Shah & Peterson (1960) and further explained by Jenekhe & Schuldt (1984).

Finally, Matar, Sisoiev & Lawrence (2008) have treated the spin-coating of thinning films on substrates with topology and flow rate modulation. Using a boundary-layer approach they showed that substrate patterning and flow rate modulation cause large waviness compared with the flat, unforced case.

Our approach to modelling spin-coating is similar to that of Reisfeld *et al.* (1991a). This work involves the study of a multi-layer film; i.e. there is a free surface and an internal interface between two fluids. Our treatment of the dynamics of the multi-layer system also closely follows the works of Danov *et al.* (1998), Pototsky *et al.* (2005) and Fisher & Golovin (2005). Although the notation is different in these multi-layer approaches the models are similar and provide the appropriate conditions at interfaces.

## 2. The model

### 2.1. Governing equations

Consider an isothermal system consisting of two immiscible, incompressible thin liquid films, one lying on top of the other, on a rigid, rotating substrate with an inviscid, passive gas phase above the layered liquids. The lower liquid film is in contact with the substrate and is designated as liquid 1, and the liquid on top is designated as liquid 2 (see figure 1). In a polar cylindrical coordinate system  $(r, \theta, z)$  the origin is placed along the axis of rotation at the substrate–liquid 1 interface (hereafter referred to as the

substrate surface) and  $z$  is perpendicular to the substrate surface. The rigid substrate surface is flat, but the liquid–gas interface ( $z = h^{(2)}(t, r, \theta, z)$ , hereafter referred to as the free surface) and the liquid–liquid interface ( $z = h^{(1)}(t, r, \theta, z)$ , hereafter referred to as the internal surface) can be any shape.

The equations governing the components of the liquid velocity  $\mathbf{v}^{(i)}(r, \theta, z, t) = (u^{(i)}(r, \theta, z, t), v^{(i)}(r, \theta, z, t), w^{(i)}(r, \theta, z, t))$  and the pressure  $p^{(i)}(r, \theta, z, t)$  in the  $i$  ( $=1, 2$ ) liquid films are the equations of motion,

$$\hat{\rho}^{(i)} \left( \frac{\partial \mathbf{v}^{(i)}}{\partial t} + \mathbf{v}^{(i)} \cdot \nabla \mathbf{v}^{(i)} \right) = -\nabla p^{(i)} - \nabla \phi^{(i)} + \hat{\eta}^{(i)} \nabla^2 \mathbf{v}^{(i)} - \hat{\rho}^{(i)} [2\boldsymbol{\omega} \times \mathbf{v}^{(i)} + \boldsymbol{\omega} \times (\boldsymbol{\omega} \times \mathbf{r}) + \mathbf{g}], \quad (2.1)$$

and the continuity equation,

$$\nabla \cdot \mathbf{v}^{(i)} = 0, \quad (2.2)$$

where  $\hat{\rho}^{(i)}$  is the liquid density of the  $i$ th fluid;  $\hat{\eta}^{(i)}$  is the viscosity;  $\boldsymbol{\omega} = (0, 0, \omega)$  is the angular velocity;  $\mathbf{r} = (r, 0, 0)$  is the radial vector; and  $\mathbf{g} = (0, 0, g)$  is the gravitational acceleration. (Bold italic characters refer to vector quantities and bold type to higher-rank tensor quantities.) The functions  $\phi^{(i)}$  represent bulk potentials within each liquid. Such terms can arise when liquid layers become thinner than a couple of hundred nanometres when van der Waals forces become relevant. It is also noted that many thin liquid polymeric layers exhibit a range of behaviours. For example, at low shear rates the behaviour is often Newtonian; as the shear rate increases there is a transition to shear thinning, and at even higher shear rates there may be another transition to Newtonian behaviour. In these cases the viscosity can be modelled by an Ellis or Carreau law (Bird, Armstrong & Hassager 1977; Myers 2005; Charpin *et al.* 2007; Brush & Roper 2008). However, based on the results of Charpin *et al.* (2007) cited in the ‘Introduction’ we do not anticipate that including the shear rate dependence of the viscosity will dramatically change our results, particularly at low shear rates, and so the liquids will be treated as Newtonian.

There are a number of conditions imposed at the three interfaces. At the substrate surface ( $z = 0$ ) the fluid velocity vanishes,

$$\mathbf{v}^{(1)} = \mathbf{o}, \quad (2.3)$$

so that there is no slip or fluid penetration.

At the free surface,  $z = h^{(2)}(r, \theta, t)$ , there is a kinematic condition

$$J = \hat{\rho}^{(2)} (\mathbf{v}^{(2)} - \mathbf{v}^{2i}) \cdot \hat{\mathbf{n}}^{(2)}, \quad (2.4)$$

where the components of the fluid velocity are evaluated at the interface and  $\mathbf{v}^{2i}$  is the velocity of the interface and  $J$  the evaporation rate (assumed constant). The unit vector normal to the  $i$ th interface is

$$\hat{\mathbf{n}}^{(i)} = \frac{(-h_r^{(i)}, -h_\theta^{(i)}/r, 1)}{(1 + (h_r^{(i)})^2 + (h_\theta^{(i)}/r)^2)^{1/2}},$$

where the subscripts denote partial derivatives. There are also the conditions on the stress tensor  $\mathbf{D}^{(2)}$  at the free surface:

$$\hat{\mathbf{n}}^{(2)} \cdot \mathbf{D}^{(2)} \cdot \hat{\mathbf{n}}^{(2)} = (p^{(2)} - p_G) + \sigma^{(2)} K^{(2)}. \quad (2.5)$$

Here, the effect of vapour recoil, which can occur when there is phase transformation (Burelbach, Bankoff & Davis 1988), has been neglected. In addition,

$$\hat{\mathbf{t}}^{(2j)} \cdot \mathbf{D}^{(2)} \cdot \hat{\mathbf{n}}^{(2)} = 0, \quad (2.6)$$

where

$$\mathbf{D}^{(2)} \equiv \hat{\eta}^{(2)}(\nabla \mathbf{v}^{(2)} + (\nabla \mathbf{v}^{(2)})^T); \quad (2.7)$$

$\hat{\mathbf{t}}^{(2j)}$  ( $j = 1, 2$ ) are tangential vectors at the free surface;  $p_G$  and  $\rho_G$  are the hydrostatic pressure and density in the overlying vapour, respectively;  $\sigma^{(2)}$  is the surface tension of the free surface; and  $K^{(2)}$  is the mean curvature of the free surface. Equation (2.6) implies that Marangoni effects are not considered.

At the internal interface, conditions include the continuity of fluid velocity,

$$\mathbf{v}^{(1)} = \mathbf{v}^{(2)}, \quad (2.8)$$

the kinematic condition,

$$\hat{\rho}^{(1)}(\mathbf{v}^{(1)} - \mathbf{v}^{li}) \cdot \hat{\mathbf{n}}^{(1)} = 0, \quad (2.9)$$

and the jump in the normal component of the stress tensor,

$$[\hat{\mathbf{n}}^{(1)} \cdot \mathbf{D}^{(i)} \cdot \hat{\mathbf{n}}^{(1)}]_{i=1}^{i=2} = (p^{(1)} - p^{(2)}) \hat{\mathbf{n}}^{(1)} + \sigma^{(1)} K^{(1)}, \quad (2.10)$$

and in the tangential components,

$$[\hat{\mathbf{t}}^{(1j)} \cdot \mathbf{D}^{(i)} \cdot \hat{\mathbf{n}}^{(1)}]_{i=1}^{i=2} = 0 \quad (2.11)$$

( $j = 1, 2$ ), where the brackets refer to the difference in the values between the upper liquid layer (2) and the lower liquid layer (1) of the quantity inside the brackets.

Finally there are the lateral conditions. In this work only axisymmetric solutions are calculated, and this requires all shape functions, fluid velocities and the pressure to have vanishing radial derivatives at the origin and to be finite there. In the far field at large  $r$  we assume that the interface remains flat. More details will be provided in the discussion of the calculations presented below.

### 3. Scaling

The governing equations and boundary conditions are non-dimensionalized using scalings adapted from Reisfeld *et al.* (1991a). It is also convenient to define  $p^{(i)*} = p^{(i)} + \phi^{(i)}$  and substitute for  $p^{(i)}$  in the interface conditions. The superscript '\*' is then dropped. In the present configuration, when considering non-retarded van der Waals forces only, evaluation of the potentials gives

$$\phi^{(1)} = \frac{A_1}{6\pi(h^{(1)})^3} + \frac{A_i}{6\pi(h^{(2)})^3} \quad (3.1)$$

and

$$\phi^{(2)} = \frac{A_2}{6\pi(h^{(2)} - h^{(1)})^3} + \frac{A_i}{6\pi(h^{(2)})^3} \quad (3.2)$$

which are to be used in the jump conditions for the normal component of the stress tensor. The coefficients  $A_1$ ,  $A_2$  and  $A_i$  are Hamaker constants representing the interactions between the internal and substrate interfaces, the internal interface

and the free surface and the free surface and the substrate interface, respectively (Israelachvili 1991; Danov *et al.* 1998; Pototsky *et al.* 2005).

The characteristic length scales for radial and vertical directions are the disk radius  $L$  and initial mean film thickness  $h_0$ , respectively. The density and viscosity are scaled to the values  $\rho_0$  and  $\eta_0$  to be chosen later (from which the scale for the kinematic viscosity is  $\nu_0 = \eta_0/\rho_0$ ). For convenience, these may be taken to be the parameters of one of the layer fluids. The substrate rotation rate is a constant value  $\omega$ . The radial velocity scale is  $U_0 = \omega^2 L h_0^2 / \nu_0$ ; the azimuthal velocity scale is  $V_0 = U_0 \omega h_0^2 / \nu_0$ ; and the vertical velocity scale is  $W_0 = U_0 h_0 / L$ . The pressure scale is  $P_0 = \rho_0 \omega^2 L^2$ ,  $\Phi^{(i)} \equiv \phi^{(i)} / P_0$ , and the time scale is  $T_0 = L / U_0$ . Scaled time and all scaled lengths, velocities and pressures are represented in upper case.

After scaling, the governing equations for layer  $i$  in component form become

$$\begin{aligned} \epsilon Re \left( \frac{\partial U}{\partial T} + U \frac{\partial U}{\partial R} + W \frac{\partial U}{\partial Z} \right) &= -\frac{1}{\rho^{(i)}} \frac{\partial P}{\partial R} + \nu^{(i)} \epsilon^2 \left[ \frac{1}{R} (RU)_R \right]_R \\ &\quad + \nu^{(i)} \frac{\partial^2 U}{\partial Z^2} + 2\epsilon Re V + R + \epsilon^2 Re^2 \frac{V^2}{R}, \end{aligned} \quad (3.3)$$

$$\epsilon Re \left( \frac{\partial V}{\partial T} + U \frac{\partial V}{\partial R} + W \frac{\partial V}{\partial Z} + \frac{UV}{R} \right) = \nu^{(i)} \frac{\partial^2 V}{\partial Z^2} + \epsilon^2 \nu^{(i)} \frac{\partial}{\partial R} \left[ \frac{1}{R} \frac{\partial (RV)}{\partial R} \right]_R - 2U, \quad (3.4)$$

$$\begin{aligned} \epsilon^3 Re \left( \frac{\partial W}{\partial T} + U \frac{\partial W}{\partial R} + W \frac{\partial W}{\partial Z} \right) &= -\frac{1}{\rho^{(i)}} \frac{\partial P}{\partial Z} + \epsilon^2 \nu^{(i)} \frac{\partial^2 W}{\partial Z^2} + \epsilon^4 \nu^{(i)} \left[ \frac{1}{R} \frac{\partial}{\partial R} \left( R \frac{\partial W}{\partial R} \right) \right], \\ &\quad (3.5) \end{aligned}$$

$$\frac{1}{R} \frac{\partial (RU)}{\partial R} + \frac{\partial W}{\partial Z} = 0, \quad (3.6)$$

where the dimensionless parameters that appear are the aspect ratio  $\epsilon = h_0/L$  and the Reynolds number  $Re = U_0 h_0 / \nu_0$ , and for the  $i$ th layer the dimensionless density  $\rho^{(i)} = \hat{\rho}^{(i)} / \rho_0$ , the dimensionless viscosity  $\eta^{(i)} = \hat{\eta}^{(i)} / \eta_0$  and the dimensionless kinematic viscosity  $\nu^{(i)} = \hat{\nu}^{(i)} / \nu_0$ . Gravitational effects are now assumed negligible.

At the surface of the substrate,

$$U^{(1)} = 0, \quad (3.7)$$

$$V^{(1)} = 0, \quad (3.8)$$

$$W^{(1)} = 0. \quad (3.9)$$

The scaled boundary conditions at the internal interface are

$$U^{(1)} = U^{(2)}, \quad (3.10)$$

$$V^{(1)} = V^{(2)}, \quad (3.11)$$

$$W^{(1)} = W^{(2)}, \quad (3.12)$$

$$\frac{\partial H^{(1)}}{\partial T} + U \frac{\partial H^{(1)}}{\partial R} = W^{(1)}, \quad (3.13)$$

$$\begin{aligned}
P^{(2)} - P^{(1)} - \Phi^{(2)} + \Phi^{(1)} + \frac{2\epsilon^2}{1 + \epsilon^2 \left(\frac{\partial H^{(1)}}{\partial R}\right)^2} & \left[ \left( \eta^{(1)} \frac{\partial W^{(1)}}{\partial Z} - \eta^{(2)} \frac{\partial W^{(2)}}{\partial Z} \right) \right. \\
& - \epsilon^2 \left( \frac{\partial H^{(1)}}{\partial R} \right) \left( \eta^{(1)} \frac{\partial W^{(1)}}{\partial R} - \eta^{(2)} \frac{\partial W^{(2)}}{\partial R} \right) - \left( \frac{\partial H^{(1)}}{\partial R} \right) \left( \eta^{(1)} \frac{\partial U^{(1)}}{\partial Z} - \eta^{(2)} \frac{\partial U^{(2)}}{\partial Z} \right) \\
& \left. - \epsilon^2 \left( \frac{\partial H^{(1)}}{\partial R} \right)^2 \left( \eta^{(1)} \frac{\partial U^{(1)}}{\partial R} - \eta^{(2)} \frac{\partial U^{(2)}}{\partial R} \right) \right] = \epsilon^3 C^{-1} K^{(2)}, \quad (3.14)
\end{aligned}$$

where  $C^{-1} = \sigma^{(1)}/\rho_0\omega^2 Lh_0^2$  is the Weber number,

$$\begin{aligned}
& \left[ 1 - \epsilon^2 \left( \frac{\partial H^{(1)}}{\partial R} \right)^2 \right] \left[ \eta^{(1)} \frac{\partial U^{(1)}}{\partial Z} - \eta^{(2)} \frac{\partial U^{(2)}}{\partial Z} + \epsilon^2 \left( \eta^{(1)} \frac{\partial W^{(1)}}{\partial R} - \eta^{(2)} \frac{\partial W^{(2)}}{\partial R} \right) \right] \\
& - 2\epsilon^2 \left( \frac{\partial H^{(1)}}{\partial R} \right) \left( \eta^{(1)} \frac{\partial U^{(1)}}{\partial R} - \eta^{(2)} \frac{\partial U^{(2)}}{\partial R} - \eta^{(1)} \frac{\partial W^{(1)}}{\partial Z} + \eta^{(2)} \frac{\partial W^{(2)}}{\partial Z} \right) = 0 \quad (3.15)
\end{aligned}$$

and

$$\eta^{(2)} \frac{\partial V^{(2)}}{\partial Z} - \eta^{(1)} \frac{\partial V^{(1)}}{\partial Z} + \epsilon^2 \left( \frac{\partial H^{(1)}}{\partial R} \right) \left[ \eta^{(1)} R \left( \frac{V^{(1)}}{R} \right)_R - \eta^{(2)} R \left( \frac{V^{(2)}}{R} \right)_R \right] = 0. \quad (3.16)$$

The scaled boundary conditions at the free surface are

$$\frac{\partial H^{(2)}}{\partial T} + U^{(2)} \left( \frac{\partial H^{(2)}}{\partial R} \right) + \frac{E}{\rho^{(2)}} \sqrt{1 + \epsilon^2 \left[ \frac{\partial H^{(2)}}{\partial R} \right]^2} = W^{(2)}, \quad (3.17)$$

where  $E = 3J/2\epsilon\rho_0 U_0$ ,

$$\begin{aligned}
P_G - P^{(2)} + \Phi^{(2)} + \frac{2\eta^{(2)}\epsilon^2}{1 + \epsilon^2 \left[ \frac{\partial H^{(2)}}{\partial R} \right]^2} & \left[ \frac{\partial W^{(2)}}{\partial Z} - \left( \frac{\partial H^{(2)}}{\partial R} \right) \frac{\partial U^{(2)}}{\partial Z} \right. \\
& \left. + \epsilon^2 \frac{\partial H^{(2)}}{\partial R} \left( \left( \frac{\partial H^{(2)}}{\partial R} \right) \frac{\partial U^{(2)}}{\partial R} - \frac{\partial W^{(2)}}{\partial R} \right) \right] = \epsilon^3 \bar{\sigma} C^{-1} K^{(2)} \quad (3.18)
\end{aligned}$$

in which  $\bar{\sigma} = \sigma^{(2)}/\sigma^{(1)}$ ,

$$\left( \frac{\partial U^{(2)}}{\partial Z} + \epsilon^2 \frac{\partial W^{(2)}}{\partial R} \right) \left[ 1 - \epsilon^2 \left( \frac{\partial H^{(2)}}{\partial R} \right)^2 \right] + 2\epsilon^2 \frac{\partial H^{(2)}}{\partial R} \left( \frac{\partial W^{(2)}}{\partial Z} - \frac{\partial U^{(2)}}{\partial Z} \right) = 0 \quad (3.19)$$

and

$$\frac{\partial V^{(2)}}{\partial Z} - \epsilon^2 \frac{\partial H^{(2)}}{\partial R} R \left( \frac{V^{(2)}}{R} \right)_R = 0. \quad (3.20)$$



#### 4. Derivation of evolution equations

To determine the behaviour of the films when the Reynolds number is  $O(1)$  or smaller, we expand  $U$ ,  $V$ ,  $W$  and  $P$  in powers of  $\epsilon$ ,

$$U^{(i)} = U^{(i0)} + \epsilon U^{(i1)} + \dots, \quad (4.1)$$

$$V^{(i)} = V^{(i0)} + \epsilon V^{(i1)} + \dots, \quad (4.2)$$

$$W^{(i)} = W^{(i0)} + \epsilon W^{(i1)} + \dots, \quad (4.3)$$

$$P^{(i)} = P^{(i0)} + \epsilon P^{(i1)} + \dots, \quad (4.4)$$

and substitute these expansions into (3.3)–(3.20). This leads to a sequence of equations at increasing order in  $\epsilon$ . The pair of evolution equations for the interfaces is derived at  $O(1)$  in  $\epsilon$ . The solution procedure is straightforward, and the result is the following two evolution equations for  $H^{(1)}$  and  $H^{(2)}$ :

$$\begin{aligned} \frac{\partial H^{(1)}}{\partial T} = & \left( \frac{\partial^2 P^{(10)}}{\partial R^2} + \frac{1}{R} \frac{\partial P^{(10)}}{\partial R} - 2 \right) \frac{(H^{(1)})^3}{6} - \left[ \frac{\partial C_6}{\partial R} + \frac{C_6}{R} \right] \frac{(H^{(1)})^2}{2} \\ & - \frac{\partial H^{(1)}}{\partial R} \left[ \left( \frac{\partial P^{(10)}}{\partial R} - R \right) \frac{(H^{(1)})^2}{2} + C_6 H^{(1)} \right] \end{aligned} \quad (4.5)$$

and

$$\begin{aligned} \frac{\partial H^{(2)}}{\partial T} = & C_5 - \left[ \left( \frac{\partial C_2}{\partial R} \right) + \frac{C_2}{R} \right] H^{(2)} + \left[ \frac{\partial S}{\partial R} + \frac{S}{R} \right] \frac{(H^{(2)})^3}{3} + \\ & + S \frac{\partial H^{(2)}}{\partial R} \frac{(H^{(2)})^2}{2} - \frac{\partial H^{(2)}}{\partial R} \left[ C_2 - \frac{S(H^{(2)})^2}{2} \right] - E, \end{aligned} \quad (4.6)$$

where

$$\begin{aligned} P^{(10)} = & P_G - C^{-1} \left( \frac{\partial^2 H^{(1)}}{\partial R^2} + \frac{1}{R} \frac{\partial H^{(1)}}{\partial R} \right) - \bar{\sigma} C^{-1} \left( \frac{\partial^2 H^{(2)}}{\partial R^2} + \frac{1}{R} \frac{\partial H^{(2)}}{\partial R} \right) \\ & + \frac{\hat{A}_2}{(H^{(2)})^3} + \frac{\hat{A}_1}{(H^{(1)})^3}, \end{aligned} \quad (4.7)$$

$$P^{(20)} = P_G - \bar{\sigma} C^{-1} \left( \frac{\partial^2 H^{(2)}}{\partial R^2} + \frac{1}{R} \frac{\partial H^{(2)}}{\partial R} \right) + \frac{\hat{A}_{21}}{(H^{(2)} - H^{(1)})^3} + \frac{\hat{A}_2}{(H^{(2)})^3}, \quad (4.8)$$

$$C_6 = \bar{\eta} [S(H^{(1)} - H^{(2)})] - \left( \frac{\partial P^{(10)}}{\partial R} - R \right) H^{(1)}, \quad (4.9)$$

$$S = \bar{\eta}^{-1} \left( \frac{\partial P^{(20)}}{\partial R} - \bar{\rho} R \right) H^{(1)}, \quad (4.10)$$

with  $\bar{\eta} = \eta^{(2)}/\eta^{(1)}$  and  $\bar{\rho} = \rho^{(2)}/\rho^{(1)}$ ,

$$C_2 = \left( \frac{\partial P^{(10)}}{\partial R} - R \right) \frac{(H^{(1)})^2}{2} + C_6 H^{(1)} - S \left( \frac{(H^{(1)})^2}{2} - H^{(1)} H^{(2)} \right) \quad (4.11)$$

and

$$\begin{aligned} C_5 = & \left[ \frac{\partial S}{\partial R} + \frac{S}{R} \right] \left( \frac{(H^{(1)})^3}{6} - \frac{(H^{(1)})^2}{2} H^{(2)} \right) + \left( \frac{\partial^2 C_2}{\partial R^2} + \frac{1}{R} \frac{\partial C_2}{\partial R} \right) H^{(1)} \\ & - S \frac{(H^{(1)})^2}{2} \frac{\partial H^{(2)}}{\partial R} - \left[ \frac{\partial^2 P^{(10)}}{\partial R^2} + \frac{1}{R} \frac{\partial P^{(10)}}{\partial R} - 2 \right] \frac{(H^{(1)})^3}{6} - \left[ \frac{\partial C_6}{\partial R} + \frac{C_6}{R} \right] \frac{(H^{(1)})^2}{2}. \end{aligned} \quad (4.12)$$

In the remainder of the paper, the effects of surface tension, van der Waals forces and inertia will be ignored. These effects will be the focus of future studies. Note that changes in the rotation rate affect the variable scalings and the dimensionless parameter  $E$ . The change in  $E$  with rotation rate means that the rate of mass loss (gain) because of evaporation (condensation) is changed relative to the rate at which mass is transported outward during thinning. In addition, the leading-order components of the fluid velocities in the two layers are presented in the Appendix.

For clarity, the governing equations will be rewritten in terms of the variables  $h^{(1)} = H^{(1)}$  and  $h^{(2)} = H^{(2)} - H^{(1)}$ , so that  $h^{(i)}$  now represents the ‘thickness’ of the  $i$ th layer. The simplified governing equations, written in terms of the new variables are

$$\frac{\partial h^{(1)}}{\partial T} = -\frac{1}{R} \left[ R^2 \left( \frac{\rho^{(1)} [h^{(1)}]^3}{3\eta^{(1)}} + \frac{\rho^{(2)} [h^{(1)}]^2 h^{(2)}}{2\eta^{(1)}} \right) \right]_R, \quad (4.13)$$

$$\frac{\partial h^{(2)}}{\partial T} = -\frac{1}{R} \left[ R^2 \left( \frac{\rho^{(2)} [h^{(2)}]^3}{3\eta^{(2)}} + \frac{\rho^{(1)} [h^{(1)}]^2 h^{(2)}}{2\eta^{(1)}} + \frac{\rho^{(2)} h^{(1)} [h^{(2)}]^2}{\eta^{(1)}} \right) \right]_R - \frac{E}{\rho^{(2)}}. \quad (4.14)$$

For simplicity, we choose  $\eta_0$  and  $\rho_0$  equal to the values of fluid 1; so  $\eta^{(1)} = 1$  and  $\rho^{(1)} = 1$ , leaving  $\rho^{(2)}$  and  $\eta^{(2)}$  as parameters in the following sections.

Before presenting results it is of interest to point out that there are two limits by which system (4.13)–(4.14) reduces to the single-layer result obtained in Emslie *et al.* (1958),

$$\frac{\partial h}{\partial t} = -\frac{\omega^2}{3\nu r} (r^2 h^3)_r, \quad (4.15)$$

in dimensional form, where  $\nu$  is the kinematic viscosity of the single layer and all other variables have been defined previously.

The first limit is that in which the properties of the two fluid are identical, so that  $\eta^{(1)} = \eta^{(2)}$  and  $\rho^{(1)} = \rho^{(2)}$ . Under these conditions, the system reduces to

$$\frac{\partial h^{(1)}}{\partial T} = -\frac{1}{3\nu^{(2)} R} \left[ R^2 \left( [h^{(1)}]^3 + \frac{3}{2} [h^{(1)}]^2 h^{(2)} \right) \right]_R, \quad (4.16)$$

$$\frac{\partial h^{(2)}}{\partial T} = -\frac{1}{3\nu^{(2)} R} \left[ R^2 \left( [h^{(2)}]^3 + \frac{3}{2} [h^{(1)}]^2 h^{(2)} + 3h^{(1)} [h^{(2)}]^2 \right) \right]_R - \frac{E}{\rho^{(2)}}. \quad (4.17)$$

The free surface is located at  $Z = h^{(1)} + h^{(2)} \equiv H(R, T)$ ; so the single-layer behaviour is given by

$$\begin{aligned} \frac{\partial H}{\partial T} = \frac{\partial h^{(1)}}{\partial T} + \frac{\partial h^{(2)}}{\partial T} = & -\frac{1}{3\nu^{(2)} R} \left[ R^2 \left( [h^{(1)}]^3 + 3[h^{(1)}]^2 h^{(2)} + 3h^{(1)} [h^{(2)}]^2 \right. \right. \\ & \left. \left. + [h^{(2)}]^3 \right) \right]_R - \frac{E}{\rho^{(2)}} = -\frac{1}{3\nu^{(2)} R} (R^2 H^3)_R - \frac{E}{\rho^{(2)}}. \end{aligned} \quad (4.18)$$

If there is no evaporation at the liquid–vapour interface this reduces to (4.15) on conversion to dimensional form.

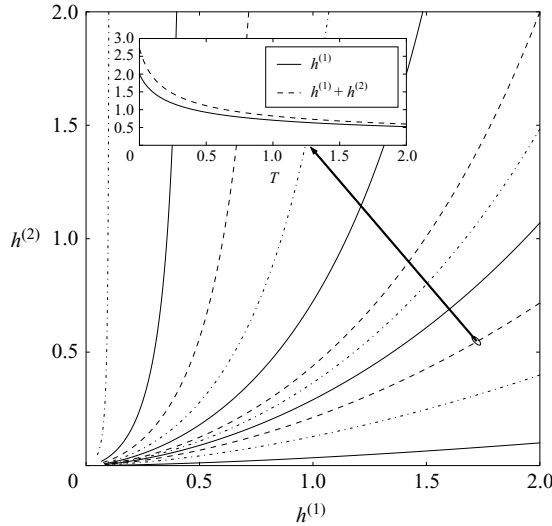


FIGURE 2. Planar solution trajectories in the  $(h^{(1)}, h^{(2)})$  plane for  $E = 0$ ,  $\eta^{(1)} = 1$ ,  $\eta^{(2)} = 0.5$ ,  $\rho^{(1)} = 1$ ,  $\rho^{(2)} = 1$ .

The second limit is an infinitely viscous lower layer. Taking  $\eta^{(1)} \rightarrow \infty$  and keeping  $\rho^{(1)}$ ,  $\rho^{(2)}$ ,  $\eta^{(2)}$ ,  $\nu^{(2)}$  finite, (4.13) and (4.14) reduce to

$$\begin{aligned} \frac{\partial h^{(1)}}{\partial T} &= 0, \\ \frac{\partial h^{(2)}}{\partial T} &= -\frac{1}{3\nu^{(2)}R} \left( R^2 [h^{(2)}]^3 \right)_R - \frac{E}{\rho^{(2)}}. \end{aligned}$$

If there is no evaporation at the liquid–vapour interface this again reduces to (4.15).

## 5. Planar solutions

Planar solutions were numerically calculated using the LSODA integrator from ODEPACK provided by Jones *et al.* (2001). We consider the three general conditions:  $E = 0$  (no evaporation),  $E > 0$  (evaporation) and  $E < 0$  (condensation). In all of the results plotted below,  $\eta^{(1)} = 1$ ,  $\rho^{(1)} = 1$ ,  $\eta^{(2)} = 0.5$  and  $\rho^{(2)} = 1$ . The solutions are plotted on the  $(h^{(1)}, h^{(2)})$  phase plane, and each trajectory on the phase plane corresponds to one thinning experiment. As  $T$  increases, the solutions initially move down and to the left along any solution trajectory in the  $(h^{(1)}, h^{(2)})$  plane. For any value of  $E$ , the lower layer always thins monotonically, requiring infinite time to reach zero thickness.

### 5.1. No evaporation ( $E = 0$ )

For zero  $E$ , both layers thin monotonically to zero as shown in figure 2, since all parameters and layer thicknesses are non-negative. The trajectories in figure 2 run from  $T = 0$  to  $T = 100$  (although it may be difficult to see in the plot, these trajectories do not reach the origin). The inset shows the behaviour of the third trajectory from the  $h^{(1)}$  axis as a function of time.

All curves are concave up, since the upper layer thins more rapidly than the lower layer, causing the trajectories to eventually approach zero along the  $h^{(1)}$  axis. Once the thickness of the upper layer is much smaller than that of the lower layer ( $h^{(2)} \ll h^{(1)}$ ),

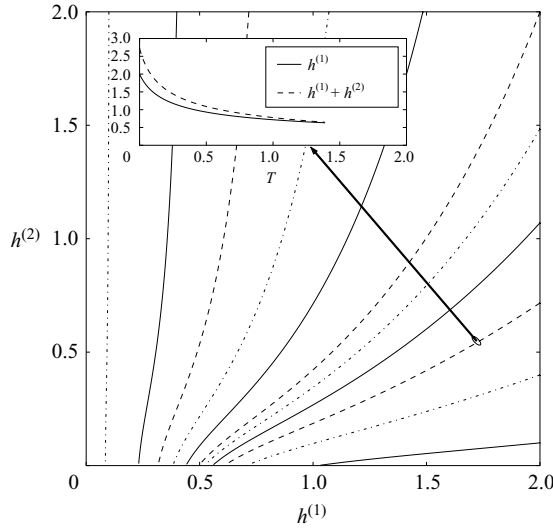


FIGURE 3. Planar solution trajectories in the  $(h^{(1)}, h^{(2)})$  plane for  $E = 0.1$ ,  $\eta^{(1)} = 1$ ,  $\eta^{(2)} = 0.5$ ,  $\rho^{(1)} = 1$ ,  $\rho^{(2)} = 1$ .

we can approximate the differential equation for  $h^{(1)}$  as

$$\frac{dh^{(1)}}{dT} = -\frac{2\rho^{(1)}}{3\eta^{(1)}} [h^{(1)}]^3. \tag{5.1}$$

This equation has a solution of the form  $h^{(1)} = 1/\sqrt{C + 2BT}$  (where  $C$  and  $B$  are constant) which reaches zero thickness as  $T \rightarrow \infty$ .

### 5.2. Evaporation ( $E > 0$ )

For positive  $E$ , the upper layer will reach zero thickness in finite time for any initial condition. Notice that for positive values of layer parameters and thicknesses,  $dh^{(2)}/dT < -E/\rho^{(2)}$ ; so the upper layer thins faster than the linear function  $\bar{h}_2 - ET/\rho^{(2)}$ , where  $\bar{h}_2$  is the value of  $h^{(2)}$  at  $T = 0$ . Therefore it reaches zero thickness at some finite time  $T_0 < \bar{h}_2\rho^{(2)}/E$ . This behaviour is seen in figure 3, with all trajectories intersecting the  $h^{(1)}$  axis at or before  $T \approx 4.51$ . As seen in the inset, the upper layer thins to zero thickness at  $T \approx 1.39$ , at which point the simulation is stopped. The curvature of the trajectories changes to concave down once the evaporation removes mass from the upper layer more rapidly than outflow at the edges. As discussed in the  $E = 0$  case, the lower layer still thins monotonically, and the approximation of the differential equation for  $h^{(1)}$  becomes exact once the upper layer thickness vanishes (assuming evaporation ceases after this time). So the lower layer would still require infinite time to reach zero thickness.

### 5.3. Condensation ( $E < 0$ )

For negative  $E$  in the upper layer, the influx of mass across the free surface will eventually balance the diminishing outflow of fluid at the right boundary, so that the upper layer approaches a steady thickness as the lower layer continues to thin because of radial drainage. This behaviour is shown in figure 4. The trajectories in figure 4 run from  $T = 0$  to  $T = 100$ .

For the given liquids, all trajectories terminate (in infinite time) at a fixed point located on the  $h^{(2)}$  axis; this is the only point for which  $dh^{(1)}/dT = dh^{(2)}/dT = 0$ . Zeros

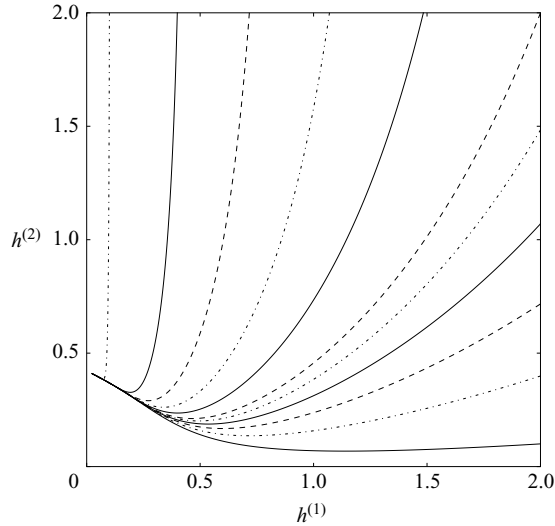


FIGURE 4. Planar solution trajectories in the  $(h^{(1)}, h^{(2)})$  plane for  $E = -0.1$ ,  $\eta^{(1)} = 1$ ,  $\eta^{(2)} = 0.5$ ,  $\rho^{(1)} = 1$ ,  $\rho^{(2)} = 1$ .

of  $dh^{(1)}/dT$  only occur along the  $h^{(2)}$  axis, whereas zeros of  $dh^{(2)}/dT$  are given by the minima of the trajectories shown in figure 4. Using (4.13) and (4.14) the intersection of these two curves can be found to determine the fixed point  $(0, h_{2eq})$ , where

$$h_{2eq} = \sqrt[3]{\frac{-3E\nu^{(2)}}{2\rho^{(2)}}}. \quad (5.2)$$

The value of  $h_{2eq}$  for the conditions shown in figure 4,  $E = -0.1$ ,  $\nu^{(2)} = 0.5$ ,  $\rho^{(2)} = 1$ , is approximately 0.422. Note that for all the trajectories shown,  $h^{(2)}$  reaches a minimum where condensation balances the drainage of the upper layer. But then the thickness of the upper layer begins to increase as the drainage in the lower and upper layers continues to reduce while the films thin further.

Finally, we have performed a linear stability analysis of the uniformly thinning films and have found no interfacial instabilities. This is consistent with the model studied that does not include inertia or attractive van der Waals forces that would cause interface perturbations to grow. Our focus in the next section is on the behaviour of larger disturbances to the liquid layers that may arise during delivery of liquid to the substrate or from other external forces.

## 6. Numerical solutions

The numerical solutions are obtained by discretizing the domain  $R \in [0, 1]$  into  $N$  equal divisions and approximating the derivatives in  $R$  from (4.13) and (4.14) using second-order accurate finite differences. The resulting system of ordinary differential equations is integrated using the LSODA integrator from ODEPACK provided by Jones *et al.* (2001). In all cases at the outer edge of the computational domain it is assumed that the evolution equations apply. At the outer boundary, the first derivatives are evaluated using a second-order accurate, one-sided finite-difference formula. This is sufficient because of the character of the partial differential equation; it is a quasi-linear hyperbolic system which has characteristic speeds that are always

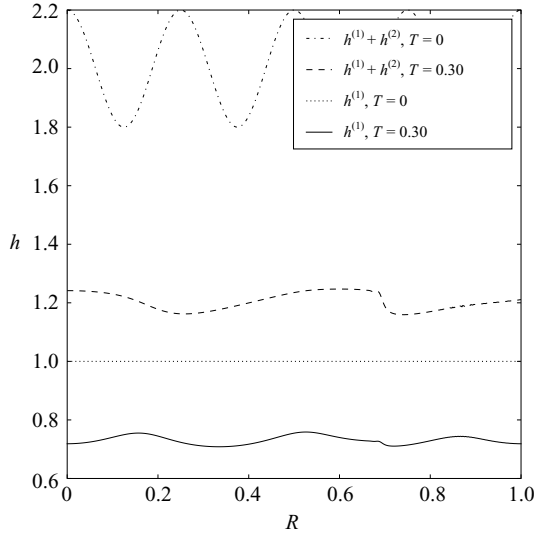


FIGURE 5. Evolution of initial conditions resembling those of Emslie *et al.* (1958), for  $T = 0$  and  $T = 0.3$ , with  $E = 0$ ,  $\eta^{(1)} = 1$ ,  $\eta^{(2)} = 0.5$ ,  $\rho^{(1)} = 1$ ,  $\rho^{(2)} = 1$ .

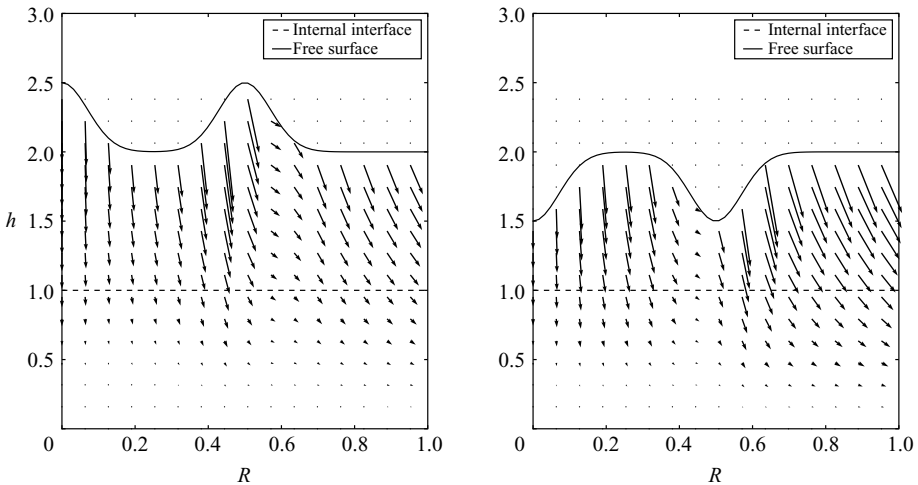


FIGURE 6. Velocity vector field for for  $E = 0$ ,  $\eta^{(1)} = 1$ ,  $\eta^{(2)} = 0.5$ ,  $\rho^{(1)} = 1$ ,  $\rho^{(2)} = 1$ , with Gaussian disturbances in the upper layer at  $R = 0$ ,  $R = 0.5$ .

positive. Thus the solution at any point depends only on points to the left at earlier times. The LSODA integrator is informed of the maximum time step that satisfies the Courant–Fredrichs–Levy condition, so that the numerical domain of dependence contains the analytical domain of dependence.

Figure 5 shows the evolution of a ripple on the free surface with a flat internal interface:  $h^{(1)} = 1$ ,  $h^{(2)} = 1 + 0.2 \cos(8\pi R)$ . The free surface at  $T = 0.3$  exhibits the same characteristics as a similar initial profile given in figure 5 in the work of Emslie *et al.* (1958). Note that the disturbances induced along the internal interface travel outward more slowly than those along the free surface. Figure 6 is simply an illustration of the flow at a given time during the evolution of two profiles having disturbances

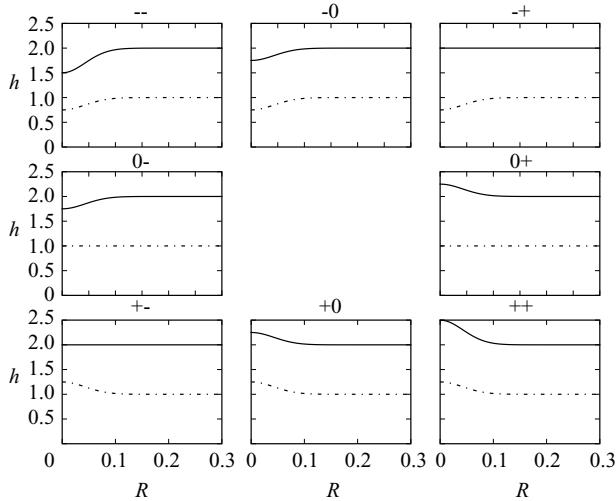


FIGURE 7. Basic set of initial conditions.

of opposite signs:  $h^{(1)} = 1$ ,  $h^{(2)} = 1 \pm 0.5[\exp(-100R^2) + \exp(-100(R - 0.5)^2)]$ . Our general observation is that behaviour of the interface disturbances is the same as observed by Emslie *et al.* (1958); they propagate outward at a speed that generally increases with  $R$  and decrease in magnitude with time.

## 7. Layer interactions

In this section we examine the differences in the evolution of the free surface and the internal interface when subject to the initial conditions enumerated in figure 7. The calculations will shed light on the influence that disturbances in one layer have on the other layer. The initial interface shapes considered include disturbances having Gaussian form (centred at  $R = 0$ ) for one or both layers, with the sign for the lower (upper) layer indicated by the first (second) symbol in the shape description. So, for example, the shape (0+) is defined by  $h^{(1)} = 1$ ,  $h^{(2)} = 1 + Ae^{-\alpha R^2}$ . Note that the classification scheme for the initial disturbances denotes changes to the ‘thickness’ of the given layer, not simply to the interface shape. Therefore, if the thickness of the lower layer alone is increased, the upper layer will exhibit an increase in height as well but not in thickness, as illustrated in figure 7. The plots in this section were produced with  $A = 0.25$ ,  $\alpha = 275$ ,  $\eta^{(1)} = 1.0$ ,  $\rho^{(1)} = 1.0$ ,  $\eta^{(2)} = 0.5$  and  $\rho^{(2)} = 1.0$ . As discussed previously, the outer boundary conditions are that the differential equations themselves are applied at  $R = 1$ . As long as the initial disturbances shown in figure 7 have not yet propagated to the outer boundary, the behaviour of the disturbed films at the boundary of the domain using this edge condition is exactly the same as in the case of thinning flat films having the same initial thickness at  $R = 1$  as the disturbed ones. Thus, in this section, calculations are continued for times over which the initial disturbances shown in figure 7 have not yet propagated to the outer boundary. An example of the difference between numerically calculated values of the thinning rate at the edge of the computational domain using this code for a non-uniform, disturbed film with the solutions for the appropriate thinning flat films is given in figure 8. In figure 8, the calculation is shown for the case in which the non-uniform film has the

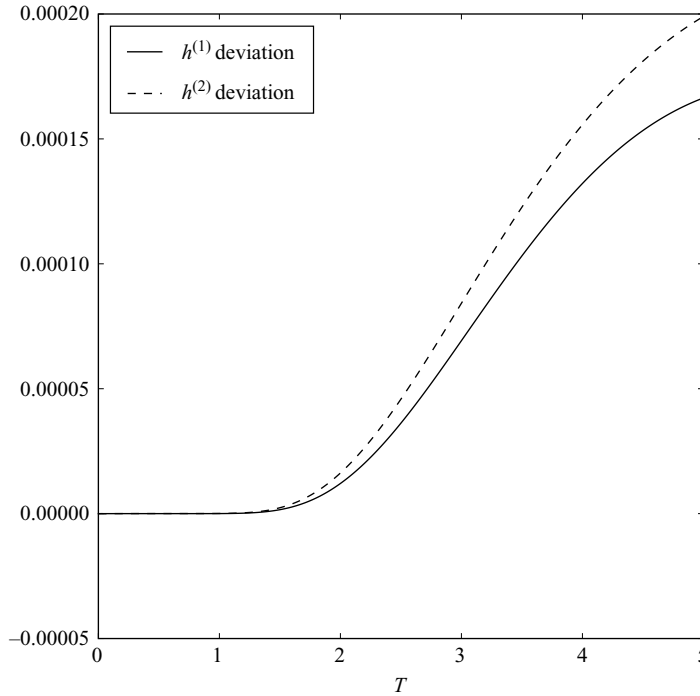


FIGURE 8. Deviation from flat state at right boundary. The initial conditions used in this calculation are given by the condition (0<sup>+</sup>) shown in figure 7.

initial condition (0<sup>+</sup>). The Gaussian disturbance does not propagate to the right edge of the domain until  $T \approx 1.1$  at which point the end conditions begin to deviate.

In order to quantify the deviation of an interface from a flat film on the interval  $R \in [0, 1]$  the following measure is defined (using  $h^{(1)}$  as an example):

$$V_0^1(h^{(1)}) = \int_0^1 \left| \frac{\partial h^{(1)}}{\partial R} \right| dR. \quad (7.1)$$

With this measure we will compare the behaviour of different initial conditions on interface evolution.

Disturbances in the lower layer have a different effect on the upper layer than do upper layer disturbances on the lower layer. For example, as shown in figure 9, a disturbance in the lower layer (initial condition (+0)) produces a maximum variation of 0.065 in the upper layer thickness, while a similar disturbance in the upper layer (0<sup>+</sup>) induces a variation of only 0.020 in the lower layer. Note that the free-surface variations for both conditions are shown in the rightmost plot to allow comparison. The variation in the free surface can be seen to decrease more rapidly for (0<sup>+</sup>) than for (+0).

Negative disturbances decay more slowly than do positive ones. As shown in figure 10, a negative disturbance in the upper layer (0<sup>-</sup>) decays much more slowly than a positive one (0<sup>+</sup>) but induces a slightly larger disturbance in the lower layer. Similarly, as shown in figure 11, (-0) decays more slowly than (+0) and induces a larger disturbance in the upper layer. Identical disturbances of opposite sign (+-), (-+) result in an initially flat free-surface boundary, but the disturbance in this



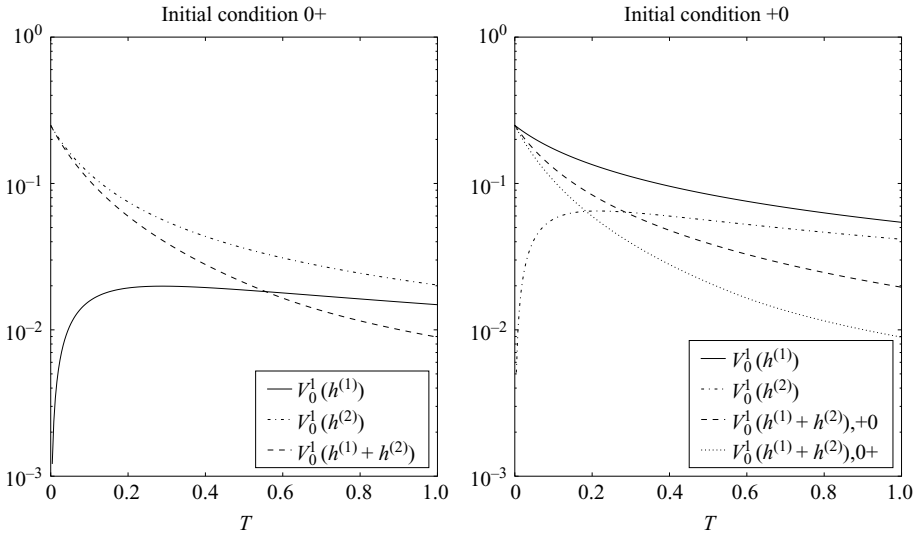


FIGURE 9. Variation of layer thicknesses and free surface for disturbances in different layers (0+ and +0).

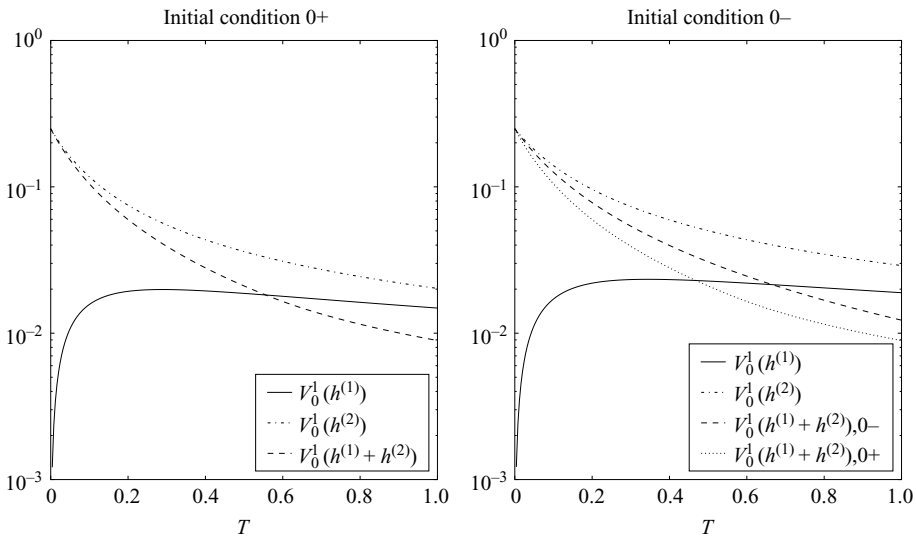


FIGURE 10. Variation of layer thicknesses and free surface for disturbances of differing sign in the upper layer (0+ and 0-).

interface is larger for the  $(-+)$  case. This can be seen in figure 12. This appears to be true for any combination of layer parameters.

In general, the results indicate that disturbances to the lower layer thickness have a greater effect on the upper layer thickness and the free surface than disturbances to the upper layer thickness have on the lower layer thickness and internal interface shape. In addition, negative disturbances tend to dissipate more slowly, and they produce a greater variation in the liquid–vapour interface than do positive disturbances.

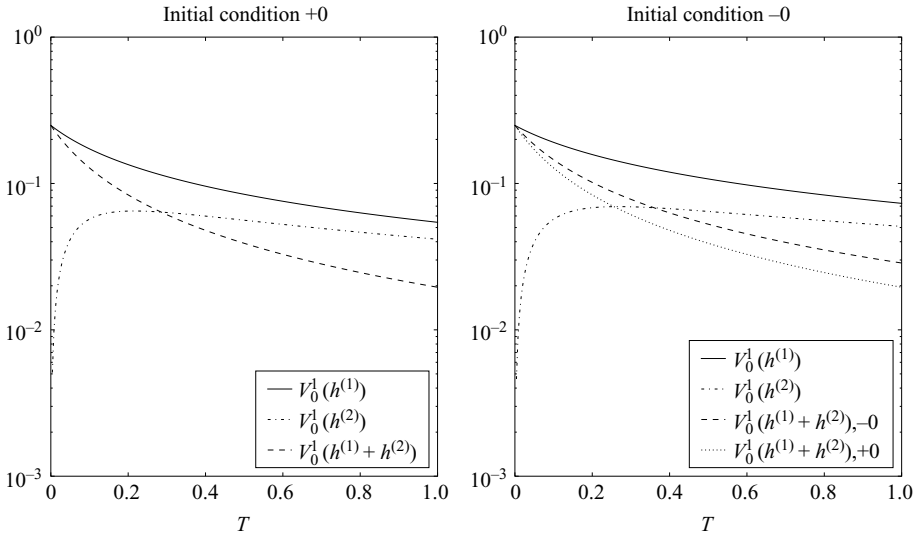


FIGURE 11. Variation of layer thicknesses and free surface for disturbances of differing sign in the lower layer (+0 and -0).

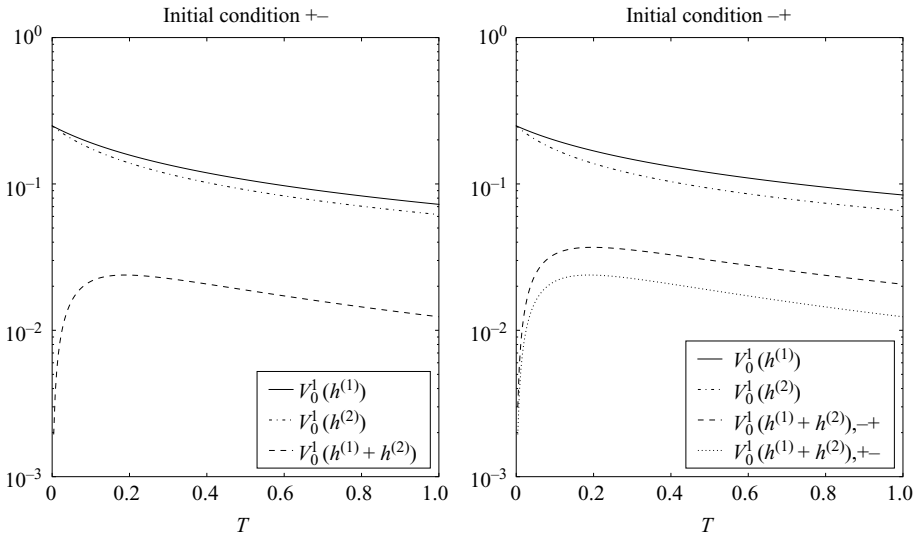


FIGURE 12. Variation of layer thicknesses and free surface for disturbances of different signs in both layers (+- and -+).

**8. Discussion**

A model of a two-layer thin liquid film on a rotating horizontal substrate is derived using lubrication theory. The system of evolution equations for the interface shapes includes the effects of van der Waals forces, capillary forces, viscous forces and mass loss or gain because of evaporation or condensation (at constant rate) at the upper free surface. Results are presented for cases that ignore gravitational, capillary and intermolecular forces.

Calculations for the evolution of flat interfaces for the three cases of no mass exchange with the overlying vapour, evaporation from the upper layer and

condensation of the upper layer show that in general, the planar solutions exhibit behaviours similar to those of the one-layer planar solutions given in Reisfeld *et al.* (1991a). For all cases the lower layer thins monotonically, reaching zero thickness only in the limit of infinite time. Without evaporation or condensation, the upper layer also takes an infinite time to thin. If evaporation is present the upper layer thins to zero thickness in finite time.

If condensation from the vapour into the upper layer is occurring, the upper layer approaches an equilibrium thickness after passing through a minimum value. Initially, the drainage rate of the upper layer fluid because of rotation is high and overwhelms the condensation rate. As the layers thin the horizontal component of the fluid velocity (and the drainage rate) in the upper layer decreases, so that eventually condensation balances the drainage, leading to a minimum upper layer thickness. As the layers thin further, the condensation rate exceeds upper layer drainage, and the upper layer thickness then increases towards its equilibrium value.

Increasing the viscosity of the upper layer at fixed rotation rate reduces the rate at which the upper layer thins, since the horizontal component of the fluid velocity and thus the drainage is decreased. This results in a reduction of the fluid velocity and thinning rate in the lower layer as well. Thus, the overall drainage rate of the layers decreases. Increasing the density of the liquids increases the thinning rate of the layers, since a denser fluid drains more rapidly at fixed rotation rate.

The variation of the interfaces from the flat state was measured. In general, disturbances to the lower layer thickness have a greater effect on the upper layer thickness and on the free surface shape than disturbances to the upper layer thickness have on the lower layer thickness and on the internal interface shape. Disturbances along the free surface propagate outward more rapidly than those along the internal interface. In general, since the fluid velocities in the upper layer are larger than those in the lower layer at a given radial distance, upper layer disturbances are advected out of the domain more quickly.

In the future additional physical effects will be included in order to examine the evolution of unstable liquid bilayers during spin-coating. This will allow comparison of the results of our model with the experimental results on the microstructural evolution of polymer blends that have been presented in the introduction.

The authors acknowledge support from the Royalty Research Fund of the University of Washington.

### Appendix: Components of the fluid velocities

$$U^{(10)} = -\frac{RZ}{2\eta^{(1)}\nu^{(1)}\nu^{(2)}} (Z\eta^{(1)}\nu^{(2)} - 2\eta^{(1)}\nu^{(2)}h^{(1)} - 2\eta^{(2)}\nu^{(1)}h^{(2)}) \quad (\text{A } 1)$$

$$U^{(20)} = \frac{R}{2\eta^{(1)}\nu^{(1)}\nu^{(2)}} (2(h^{(1)} + h^{(2)})Z\eta^{(1)}\nu^{(1)} - (\nu^{(1)} - \nu^{(2)})\eta^{(1)}[h^{(1)}]^2 - 2(\eta^{(1)} - \eta^{(2)})\nu^{(1)}h^{(1)}h^{(2)} - Z^2\eta^{(1)}\nu^{(1)}) \quad (\text{A } 2)$$

$$V^{(10)} = -\frac{RZ}{12[\eta^{(1)}]^2[\nu^{(1)}]^2[\nu^{(2)}]^2} (Z^3[\eta^{(1)}]^2[\nu^{(2)}]^2 + 8[\eta^{(1)}]^2[\nu^{(2)}]^2[h^{(1)}]^3 + 8\eta^{(1)}\eta^{(2)}[\nu^{(1)}]^2[h^{(2)}]^3 + 24\eta^{(1)}\eta^{(2)}\nu^{(1)}\nu^{(2)}[h^{(1)}]^2h^{(2)} + 24[\eta^{(2)}]^2[\nu^{(1)}]^2h^{(1)}[h^{(2)}]^2 - 4(\eta^{(1)}\nu^{(2)}h^{(1)} + \eta^{(2)}\nu^{(1)}h^{(2)})Z^2\eta^{(1)}\nu^{(2)}) \quad (\text{A } 3)$$

$$\begin{aligned}
V^{(20)} = & \frac{R}{12[\eta^{(1)}]^2[v^{(1)}]^2[v^{(2)}]^2} \left[ 4(h^{(1)} + h^{(2)})Z^3[\eta^{(1)}]^2[v^{(1)}]^2 + 8(\eta^{(1)} - \eta^{(2)})\eta^{(1)}[v^{(1)}]^2 \right. \\
& \times h^{(1)}[h^{(2)}]^3 + 24(\eta^{(1)} - \eta^{(2)})\eta^{(2)}[v^{(1)}]^2[h^{(1)}]^2[h^{(2)}]^2 - Z^4[\eta^{(1)}]^2[v^{(1)}]^2 \\
& - 4((\eta^{(1)} - 3\eta^{(2)})v^{(1)} - (3\eta^{(1)} - 5\eta^{(2)})v^{(2)})\eta^{(1)}v^{(1)}[h^{(1)}]^3h^{(2)} - ([v^{(1)}]^2 - 6v^{(1)}v^{(2)}) \\
& + 5[v^{(2)}]^2)[\eta^{(1)}]^2[h^{(1)}]^4 - 6((v^{(1)} - v^{(2)})\eta^{(1)}h^{(1)} + 2(\eta^{(1)} - \eta^{(2)})v^{(1)}h^{(2)}) \\
& \times Z^2\eta^{(1)}v^{(1)}h^{(1)} + 4((v^{(1)} - 3v^{(2)})\eta^{(1)}[h^{(1)}]^3 - 2\eta^{(1)}v^{(1)}[h^{(2)}]^3 - 6\eta^{(2)}v^{(1)}h^{(1)}[h^{(2)}]^2 \\
& \left. + 3((\eta^{(1)} - 2\eta^{(2)})v^{(1)} - \eta^{(1)}v^{(2)})[h^{(1)}]^2h^{(2)}Z\eta^{(1)}v^{(1)} \right] \quad (\text{A } 4)
\end{aligned}$$

$$\begin{aligned}
W^{(10)} = & -\frac{Z^2}{6\eta^{(1)}v^{(1)}v^{(2)}} \left( 3R\eta^{(1)}v^{(2)}\frac{\partial h^{(1)}}{\partial R} + 3R\eta^{(2)}v^{(1)}\frac{\partial h^{(2)}}{\partial R} - 2Z\eta^{(1)}v^{(2)} \right. \\
& \left. + 6\eta^{(1)}v^{(2)}h^{(1)} + 6\eta^{(2)}v^{(1)}h^{(2)} \right) \quad (\text{A } 5)
\end{aligned}$$

$$\begin{aligned}
W^{(20)} = & -\frac{1}{6\eta^{(1)}v^{(1)}v^{(2)}} \left( 3(\eta^{(1)} - \eta^{(2)})Rv^{(1)}\frac{\partial h^{(2)}}{\partial R}[h^{(1)}]^2 + 2(v^{(1)} - v^{(2)})\eta^{(1)}[h^{(1)}]^3 \right. \\
& + 6(\eta^{(1)} - \eta^{(2)})v^{(1)}[h^{(1)}]^2h^{(2)} + 3\left( R\frac{\partial h^{(1)}}{\partial R} + R\frac{\partial h^{(2)}}{\partial R} + 2h^{(1)} + 2h^{(2)} \right) Z^2\eta^{(1)}v^{(1)} \\
& - 2Z^3\eta^{(1)}v^{(1)} + 3((v^{(1)} - v^{(2)})\eta^{(1)}h^{(1)} + 2(\eta^{(1)} - \eta^{(2)})v^{(1)}h^{(2)})Rh^{(1)}\frac{\partial h^{(1)}}{\partial R} \\
& - 6\left( (\eta^{(1)} - \eta^{(2)})Rv^{(1)}\frac{\partial h^{(2)}}{\partial R}h^{(1)} + (v^{(1)} - v^{(2)})\eta^{(1)}[h^{(1)}]^2 + 2(\eta^{(1)} - \eta^{(2)})v^{(1)}h^{(1)}h^{(2)} \right. \\
& \left. + ((v^{(1)} - v^{(2)})\eta^{(1)}h^{(1)} + (\eta^{(1)} - \eta^{(2)})v^{(1)}h^{(2)})R\frac{\partial h^{(1)}}{\partial R} \right) Z \quad (\text{A } 6)
\end{aligned}$$

## REFERENCES

- ACRIVOS, A., SHAH, M. J. & PETERSEN, E. E. 1960 On the flow of a non-Newtonian liquid on a rotating disk. *J. Appl. Phys.* **31**, 963–968.
- BIRD, R. B., ARMSTRONG, R. C. & HASSAGER, O. 1977 *Dynamics of Polymeric Fluids, Vol. I – Fluid Mechanics*. John Wiley.
- BJORSTROM, C. M., NILSSON, S., BERNASIK, A., BUDKOWSKIC, A., ANDERSSON, M., MAGNUSSON, K. O. & MOONS, E. 2007 Vertical phase separation in spin-coated films of a low bandgap polyfluorene/PCBM blend. Effects of specific substrate interaction. *Appl. Surface Sci.* **253** (8), 3906–3912.
- BRUSH, L. N. & ROPER, S. M. 2008 The thinning of lamella in surfactant-free foams with non-Newtonian liquid phase. *J. Fluid. Mech.* **616**, 235–262.
- BURELBACH, J. P., BANKOFF, S. G. & DAVIS, S. H. 1988 Nonlinear stability of evaporating/condensing liquid films. *J. Fluid. Mech.* **195**, 463–494.
- CASTRO, F. A., GRAEFF, C. F. O., HEIER, J. & HANY, R. 2007 Interface morphology snapshots of vertically segregated thin films of semiconducting polymer/polystyrene blends. *Polymer* **48**, 2380–2386.
- CHARPIN, J. P. F., LOMBE, M. & MYERS, T. G. 2007 Spin coating of non-Newtonian fluids with a moving front. *Phys. Rev. E* **76**, 016312.
- CRASTER, R. V. & MATAR, O. K. 2009 Dynamics and stability of thin liquid films. *Rev. Mod. Phys.* **81**, 1131–1198.
- DANOV, K. D., PAUNOV, V. N., ALLEBORN, N., RASZILLER, H. & DURST, F. 1998 Stability of evaporating two-layered liquid film in the presence of surfactant. Part I. The equations of lubrication approximation. *Chem. Engng Sci.* **53** (15), 2809–2822.

- DAVIS, S. H. 2000 *Perspectives in Fluid Dynamics: A Collective Introduction to Current Research* (ed. G. K. Batchelor, H. K. Moffatt & M. G. Worster), chapter 1, pp. 1–51. Cambridge University Press.
- DUSSAN, V. E. B. 1979 On the spreading of liquids on solid surfaces: static and dynamic contact lines. *Annu. Rev. Fluid. Mech.* **11**, 371–400.
- DUSSAN, V. E. B. & DAVIS, S. H. 1974 On the motion of fluid-fluid interface along a solid surface. *J. Fluid Mech.* **65**, 71–95.
- EHRHARD, P. & DAVIS, S. H. 1991 Non-isothermal spreading of liquid drops on horizontal plates. *J. Fluid Mech.* **229**, 365–388.
- EMSLIE, A. G., BONNER, F. T., & PECK, L. G. 1958 Flow of a viscous liquid on a rotating disk. *J. Appl. Phys.* **29** (5), 858–862.
- ERNEUX, E. & DAVIS, S. H. 1993 Nonlinear rupture of free films. *Phys. Fluids A* **5**, 1117–1122.
- FISHER, L. S. & GOLOVIN, A. A. 2005 Nonlinear stability analysis of a two-layer thin liquid film: dewetting and autophobic behavior. *J. Colloid Interface Sci.* **291**, 515–528.
- GAO, P. & LU, X. 2008 Mechanism of the long-wave inertialess instability of a two-layer film flow. *J. Fluid Mech.* **608**, 379–391.
- HALLS, J. J. M., WALSH, C. A., GREENHAM, N. C., MARSEGILA, E. A., FRIEND, R. H., MORATTI, S. C. & HOLMES, A. B. 1995 Efficient photodiodes from interpenetrating polymer networks. *Nature* **376**, 498–500.
- HERIOT, S. Y. & JONES, R. A. L. 2005 An interfacial instability in a transient wetting layer leads to lateral phase separation in thin spin-cast polymer-blend films. *Nature Mat.* **4**, 782–786.
- ISRAELACHVILI, J. N. 1991 *Intermolecular and Surface Forces*. Academic.
- JONES, E., OLIPHANT, T., PETERSON, P., ET AL. 2001 SciPy: open source scientific tools for Python. <http://www.scipy.org>.
- JENEKHE, S. A. & SCHULDT, S. B. 1984 Coating flow of non-Newtonian fluids on a flat rotating disk. *Indus. Engng Chem. Fund.* **23**, 432–436.
- KLIAKHANDLER, I. L. & SIVASHINSKY, G. I. 1995 Kinetic alpha effect in viscosity stratified creeping flows. *Phys. Fluids* **7** (8), 1866–1871.
- KLIAKHANDLER, I. L. & SIVASHINSKY, G. I. 1996 Viscous damping and instabilities in stratified liquid film flowing down a slightly inclined plane. *Phys. Fluids* **9** (1), 23–30.
- LI, C. H. 1969 Instability of a three-layer viscous stratified fluid. *Phys. Fluids* **12**, 2473.
- MATAR, O. K., SISOEV, G. M. & LAWRENCE, C. J. 2008 Thin film flow over spinning disks: The effect of surface topography and flow rate modulation. *Chem. Engng Sci.* **63**, 2225–2232.
- MOMONIAT, E. & MASON, D. P. 1998 Investigation of the effect of the Coriolis force on a thin fluid film on a rotating disk. *Intl J. Nonlin. Mech.* **33** (6), 1069–1088.
- MYERS, T. G. 2005 Application of non-Newtonian models to thin film flow. *Phys. Rev. E* **72**, 066302.
- MYERS, T. G. & CHARPIN, J. P. F. 2001 The Effect of the Coriolis force on axisymmetric rotating thin film flows. *Intl J. Nonlin. Mech.* **36**, 629–635.
- ORON, A., DAVIS, S. H. & BANKOFF, S. G. 1997 Long-scale evolution of thin liquid films. *Rev. Mod. Phys.* **69** (3), 931–980.
- POTOTSKY, A., BESTEHORN, M., MERKT, D. & THIELE, U. 2005 Morphology changes in the evolution of liquid two-layer films. *J. Chem. Phys.* **122**, 224711.
- REISFELD, B., BANKOFF, S. G. & DAVIS, S. H. 1991a The dynamics and stability of thin liquid-films during spin-coating. Part I. Films with constant rates of evaporation or absorption. *J. Appl. Phys.* **70** (10), 5258–5266.
- REISFELD, B., BANKOFF, S. G. & DAVIS, S. H. 1991b The dynamics and stability of thin liquid-films during spin-coating. Part II. Films with unit order and large Péclet numbers. *J. Appl. Phys.* **70** (10), 5267–5277.
- SCHWARTZ, L. W. & ROY, R. V. 2004 Theoretical and numerical results for spin coating of viscous liquids. *Phys. Fluids* **16** (3), 569–584.
- SPRENGER, M., WALHEIM, S., BUDKOWSKI, A. & STEINER, U. 2003 Hierarchic structure formation in binary and ternary polymer blends. *Interface Sci.* **11**, 225–335.
- WEI, J. H., COFFEY, D. C. & GINGER, D. S. 2006 Nucleating pattern formation in spin-coated polymer blend films with nanoscale surface templates. *J. Phys. Chem. B* **110**, 24324–24330.
- WILLIAMS, M. B. & DAVIS, S. H. 1982 Non-linear theory of film rupture. *J. Colloid Interface Sci.* **90** (1), 220–228.
- YANG, F. & FORREST, S. R. 2008 Photocurrent generation in nanostructured organic solar cells. *ACS Nano* **2** (5), 1022–1032.